



TECHNICAL ARTICLE

Microstructure and Mechanical Properties of Active Gas Arc Welding between 304 Austenitic Stainless Steel and Q235B Low Carbon Steel

Jihua Liu, Xinghao Li, Yujun Zhou, Pijie Yu, Chenggang He, and Zhibiao Xu

Submitted: 9 September 2021 / Revised: 23 December 2021 / Accepted: 20 February 2022 / Published online: 23 March 2022

In the present study, metal active gas arc welding was carried out for dissimilar welding of 304 austenitic stainless steel and Q235B low carbon steel. The microstructure of the joints was investigated by using scanning electron microscopy, optical microscopy, and electron backscattered diffraction. Microhardness and tensile test results were utilized to characterize the mechanical behavior of the joints. The tensile fracture mechanism of the welded joints was explored by examining their solidification and crystallization modes. The results indicate that the weld zones of the two base metals are affected by heat input and cooling, which results in coarse grain sizes and low microhardness values. The heat-affected zones contain complex microstructure, including Widmanstatten structure, ferrite, and pearlite. Energy-dispersive spectroscopy analysis shows an obvious elemental transition zone at the fusion line on the Q235B side of a joint. The microhardness is lowest at the weld seam of a joint and highest at the fusion line on the carbon steel side due to martensitic structure. The solidification and crystallization modes of the welded joints are discussed and combined with the analysis of microstructure and mechanical properties. The results show that due to the difference in the thermal conductivities of the two base metals, a grain boundary convergence zone forms in the weld center after solidification and crystallization of the weld metal, resulting in fracture at the weld center in tensile testing.

Keywords low carbon steel, MAG, mechanical properties, microstructure, solidification, stainless steel

1. Introduction

Due to its good plasticity, high strength, and excellent corrosion resistance, stainless steel is widely used in various fields. However, the production cost of stainless steel is much higher than that of carbon steel, and dissimilar welding of stainless steel and typical low carbon steel is frequently used to make mechanical structures. Many studies of dissimilar steel welding have been carried out by using the advanced technologies of inert tungsten gas welding (TIG), friction stir welding (FSW), and laser beam welding (LBW).

Arc-assisted activated TIG welding (AA-TIG) was adopted to weld 12Cr2Mo1R heat-resistant steel and 06Cr18Ni11Ti austenitic stainless steel (Ref 1), and the microstructure and mechanical properties were analyzed. The results indicated that when ER309L welding wire was used, martensite and ferrite structures formed and mechanical properties and corrosion resistance improved. TIG welding was used by Khalifeh et al. (Ref 2) to join austenitic stainless steel (AISI 304L) and ferritic carbon steel (St37). In a comparison of four austenitic filler

metals, ER308L, ER309L, ER316L, and ER310, the impact toughness of the weldments decreased with increasing delta ferrite content in the weld metals. FSW welding was performed by Wang et al. (Ref 3) on typical 304 stainless steel and Q235 low carbon steel, and the microstructure of the welded joint as well as the mechanical properties was studied. The results showed that the tensile strength of the welded joints and SZ (stirring zone) were higher than that of the Q235 base metal. For 304 stainless steel and Q235 low carbon steel, mechanical bonding and metallurgical bonding were observed. St37 low carbon steel was welded with 304 stainless steel by Khodadadi et al. (Ref 4). They found two failure modes, including shear failure and shear/tension mixed failure, and the failure modes were determined not only by rotational speed but also by bonding length (weld nugget size) and crack propagation path. Austenite/martensite was welded by Zhang et al. (Ref 5) by using laser beam welding, and the process was optimized by using the Box–Behnken design method. The results indicated that no visible cracks formed at the heat-affected zone of austenitic stainless steel, and the fracture force of the weld joint was successfully enhanced. AISI 420 martensitic stainless steel was applied to AISI 2205 duplex stainless steel sheets with laser welding by Köse et al. (Ref 6). The results showed that the main reason for the decrease in the mechanical strength of the welded joints was the formation of macroscopic pores and carbides.

As reviewed above, the quality, speed, and productivity of welding can be greatly improved by using laser welding, friction stirring, and other welding technologies. However, it is still difficult to broadly apply these techniques due to their complex processes, expensive equipment, demanding require-

Jihua Liu, Xinghao Li, Yujun Zhou, Pijie Yu, Chenggang He, and Zhibiao Xu, School of Rail Transit, Wuyi University, Jiangmen 529020, China. Contact e-mail: hechengan@126.com.

ments for welding assembly precision, and poor adaptability. Nevertheless, metal active gas arc welding (MAG) has been widely used in the manufacturing of pressure vessels, machinery, ships, locomotives, and vehicles due to its advantages of low cost, robust adaptability, and easy automation. For example, typical components such as lifting lugs of rail vehicle cabinets are manufactured by using MAG for dissimilar welding of steels in Chinese Rolling Stock Company. However, previous studies of MAG welding have mainly focused on welding two pieces of the same material (Ref 7–9), and only a few researchers have paid attention to the MAG welding of dissimilar steels (Ref 10, 11). Moreover, studies on dissimilar MAG welding were carried out under specific working conditions, and dissimilar MAG welding of stainless steel and carbon steel was rarely reported, especially for 304 austenitic stainless steel and Q235B low carbon steel. Therefore, it is particularly important to study the microstructures and mechanical properties of dissimilar MAG welded joints of 304 austenitic stainless steel and Q235B low carbon steel.

As MAG welding is a typical fusion welding process, the materials of welded joints always undergo melting and solidification, which greatly influence the grain growth behavior, thus ultimately determining the performance of the welded joints. Many studies have been conducted on the solidification and crystallization behaviors of fusion welded joints. The TIG welding process was adopted by Singh et al. (Ref 12) to weld SS304 and medium carbon steel En8, and the effects of the welding process parameters on the weld and mechanical properties were studied. The results indicated that the heat input greatly influenced the solidification rate, thus resulting in differences in weld microstructure. Research using finite element analysis and comparative experimental analysis (Ref 13, 14) showed that heat input and cooling rate during the welding process affected the growth, sizes, and distributions of grains. Changing the heat input in the welding process can influence the mechanical properties (hardness, residual stress, etc.) of the welded joint.

One of the main aims of this research was to evaluate the reliability and performance of dissimilar MAG welded joints of 304 stainless steel and Q235B low carbon steel, thus enriching the reliability database of information about different forms of welded joints for typical components, such as lifting lugs for rail vehicle cabinets. Moreover, the relationship between the tensile fracture mechanism and solidification and crystallization behavior of dissimilar welding joints was analyzed in detail in terms of the cooling rate. The results of this paper can provide a theoretical and technical basis for field applications of MAG welding of stainless and carbon steels.

2. Materials and Test Methods

2.1 Materials and Welding Methods

In this study, a Phonix TPS5000 complete digital MIG welding machine was used to weld 304 austenitic stainless steel and Q235B low carbon steel. A diagram of the welding process of dissimilar steels and the welding parameters are shown in Fig. 1 and Table 1, respectively. Steel plates with dimensions of 500 × 200 × 4 mm were utilized, and GMS-309L was chosen as the filler wire during welding. 309L is the preferred filler material for connecting austenitic stainless steel to carbon steel

because it can retain ferrite residue in the weld and prevent hot cracking. The chemical compositions and mechanical properties of the base metals and the weld metal are shown in Tables 2 and 3, respectively.

2.2 Test Methods

The microstructure of the joints was observed perpendicular to the welding direction (WD). After rough grinding and fine grinding with different grades of waterproof sandpaper, diamond grinding paste was used for mechanical polishing. Aqua regia (HCl:HNO₃ = 3:1) was used for metallographic corrosion of 304 base material and weld seams, and the Q235B low carbon steel was corroded by alcohol containing 4% nitric solution. A VHX-6000 3D microscope with a super wide depth of field was used for optical microscopy (OM), and a Sigma500 field-emission scanning electron microscope was utilized to observe the microstructure of dissimilar 304-Q235B steel welded joints. The elemental distribution was analyzed by scanning electron microscopy (SEM) with an Oxford-Instruments X-Max N large area SDD spectrometer. Electron backscattering diffraction (EBSD) samples were cut vertically to WD and electropolished with 10% perchloric acid solution and 90% ethanol at 25 V and -35°C. EBSD diagrams were acquired by using a fully automated HKL-EBSD system interfaced with a ZEISS MERLIN Compact field-emission SEM.

An HVT-1000 microhardness tester was adopted to test the microhardness of the joints, and a load of 500 g and a dwell time of 10 s were used. Indentations along the horizontal direction and the vertical direction were 150 and 200 μm wide, respectively. Moreover, the microhardness data were analyzed by matrix algorithms, and microhardness distribution maps were obtained. As shown in Fig. 2, every tensile specimen was cut in a gauge section dimension. The tensile tests were carried out by an electronic universal testing machine (model DNS300), and the stretching speed was 5 mm/min. After the tensile tests, the fracture morphologies were observed by SEM.

3. Results

3.1 Microstructure of the Welded Joints

Figure 3(a) depicts the microscopic section morphology of a welded joint of dissimilar 304-Q235B steels. The welding joint is complete, and there are no defects, such as slag inclusions, crack porosities, nonpenetration, and nonfusion. Figure 3(b) and (c) shows that the weld microstructure is organized in worm-like domains, skeletal ferrite is distributed in austenite grains, and the amount of δ-ferrite on the 304 side of the weld is greater than that on the Q235B side.

The microstructure of the 304 austenitic stainless steel side of the welded joints and some local microstructures are depicted in Fig. 4. As shown in Fig. 4(b), BM304 has a typical austenitic structure with twin structure in some grains and slight ferrite mixing at the austenitic grain boundaries. Figure 4(c) shows that there is a large number of dendritic ferrites parallel to the RD (rolling direction) at the austenite grain boundary. At a location approximately 500 μm away from the fusion line, the grain size is much larger than that of the base metal, which resulted from the higher peak temperature and the lower thermal conductivity of the base metal, as shown in Fig. 4(d).

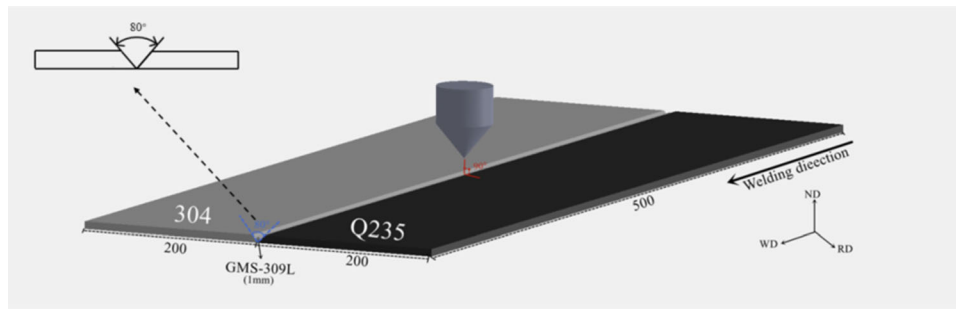


Fig. 1 Schematic of MAG

Table 1 Parameters of MAG welding

Methods	Wire Diameter, mm	Current, A	Speed, cm/min	Shielding gas	Gas flow, L/min
MAG	1	160	40	98%Ar+2%O2	10

Table 2 Chemical compositions of materials

Materials	C%	Si%	Mn%	P%	S%	Cr%	Ni%	Mo%	Ti%	Fe
304	0.04	0.51	1.17	0.026	0.51	18.24	8.00			Bal.
Q235B	0.20	0.12	0.21	0.016	0.12					Bal.
GMS-309L	0.21	0.81	2.03	0.016	0.012	23.78	13.78	0.01	0.01	Bal.

Table 3 Mechanical properties of materials

Materials	Tensile strength Rm, MPa	yield strength σ_s , MPa	Elongation%	Reduction of area%
304	520 Min	205 Min	40 Min	60 Min
Q235B	375-500	235 Min	26 Min	50 Min
309L	510 Min	205 Min	25 Min	60 Min

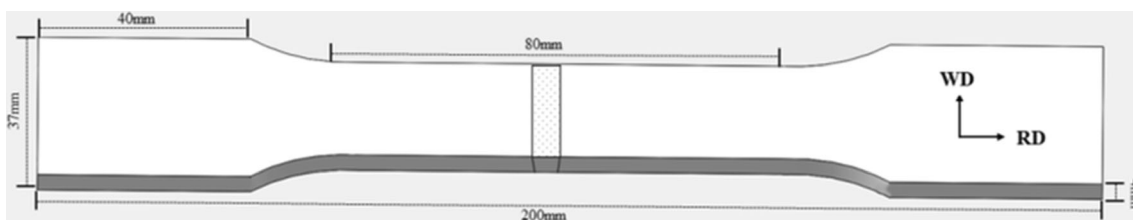
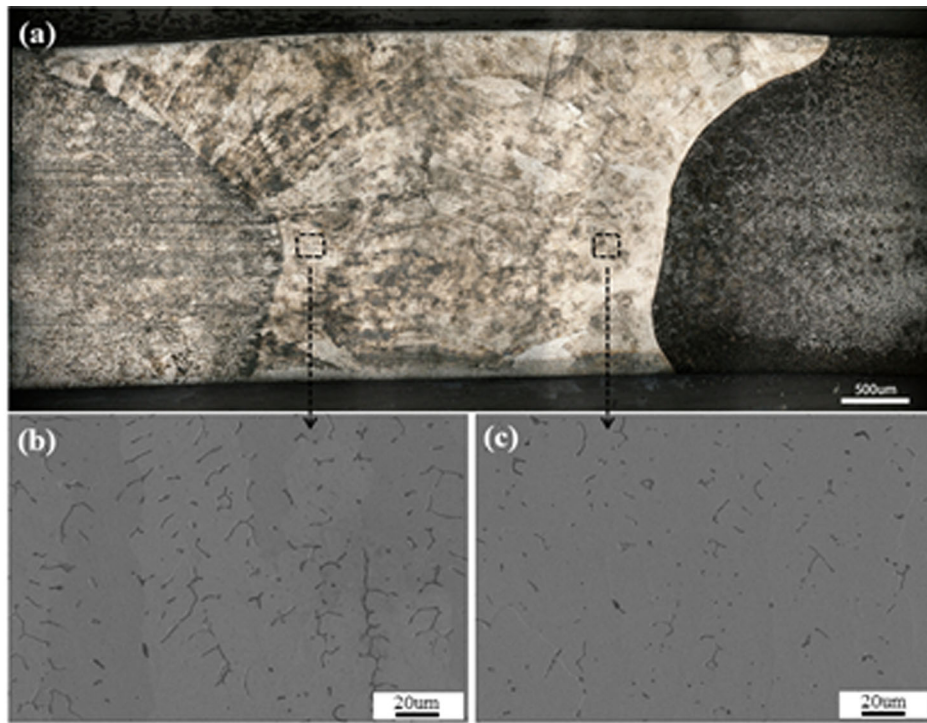


Fig. 2 Schematic diagram of tensile sample

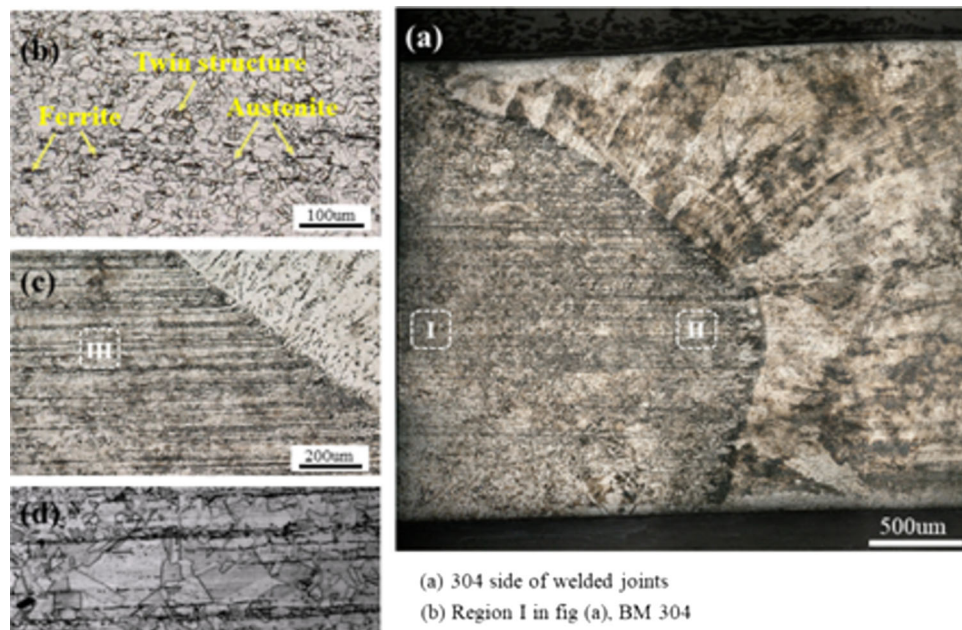
The microstructure on the Q235B carbon steel side in a welded joint and some local microstructures are depicted in Fig. 5. The structures in the heat-affected zone transform rapidly with distance from the fusion line due to differences in heat input and heat conduction. In the CGHAZQ235B region, the structure is complex, and the distribution is uneven, as shown in Fig. 5(b) and (c). In region 1, there is martensitic microstructure at the pearlite grain boundary, and part of the ferrite appears in the form of acicular ferrite. In region 2, unevenly distributed pearlite and ferrite are observed, as well as

a small amount of acicular ferrite. As shown in Fig. 5(d), the pearlite and ferrite in the FGHAZQ235B region are notably refined by grains, and the width of this region is quite small at approximately 500 μm . In the IGHZAQ235 region approximately 3 mm from the fusion line, the ferrite grains display nonuniform sizes, and the pearlite grain refinement phenomenon is clearly observed, as shown in Fig. 5(e). A typical ferrite and pearlite structure is observed at BMQ235B, as presented in Fig. 5(f).



(a) Microstructure of the weld (b) OM of the weld near 304 (c) OM of the weld near Q235B

Fig. 3 Microscopic images of the welded joint



(a) 304 side of welded joints
(b) Region I in fig (a), BM 304

Fig. 4 Microstructure of a welded joint on the 304 austenitic stainless steel side

As the chemical composition and structure of the austenitic welding wire and base material are different in dissimilar steel melting welding, the fusion zone microstructure needs to be analyzed further, especially on the carbon steel side. Figure 6(a) shows the fusion line of 304 austenitic steel. No apparent columnar grain characteristics are present in the austenite matrix, and the ferrite distribution in the austenite matrix is discontinuous without orientation. As shown in Fig. 6(b), a

prominent black belt area is present on the fusion line of Q235B carbon steel. A similar black belt area composed of hard and brittle phases was referred to as a C-rich layer in previous studies (Ref 15, 16) because of the enrichment of elemental C in this interface. A serrated morphology parallel to the black belt area strip has a typical martensite lath structure perpendicular to the weld; a similar structure was identified as a type II grain boundary in prior studies (Ref 17, 18).

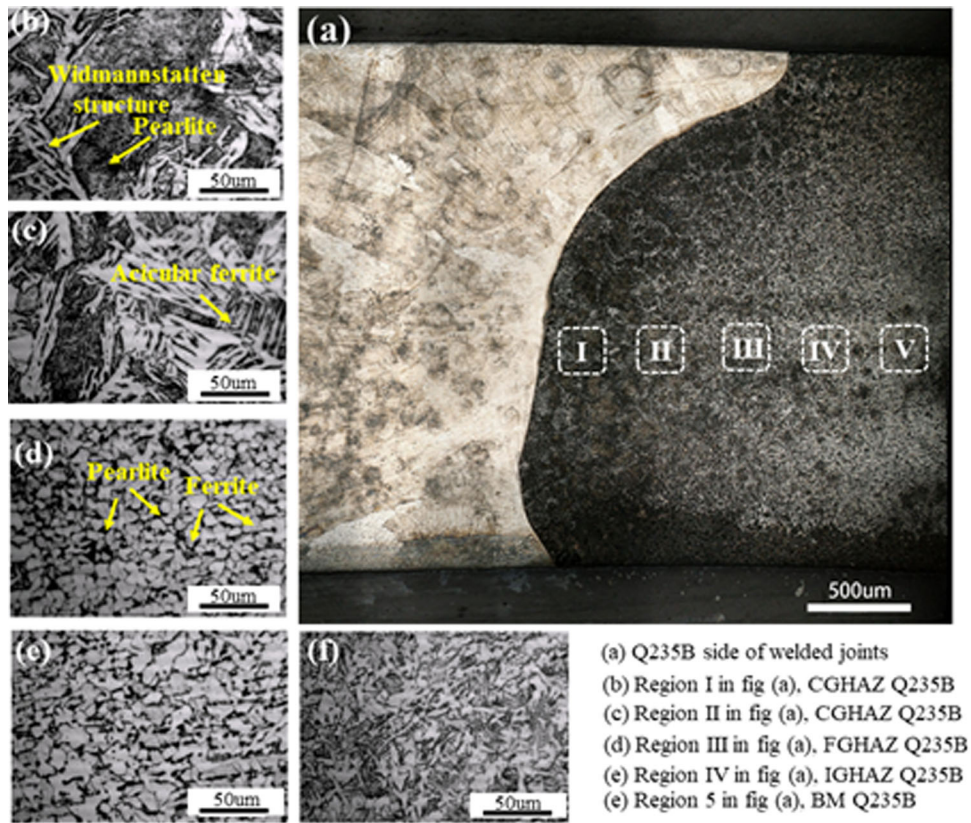


Fig. 5 Microstructure of a welded joint on the Q235B low carbon steel side

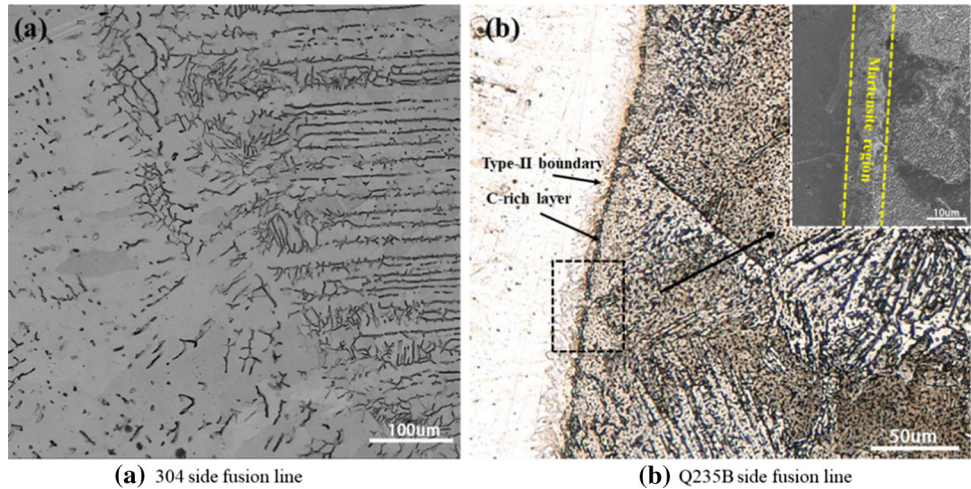


Fig. 6 Microstructure of the fusion line

3.2 Elements and Structure of the Welded Joints

The characteristics of the grain distributions at different positions in a welded joint are depicted in Fig. 7. The grain size at the weld seam is relatively large, the grains meet in the middle of the weld, and the grain boundaries at the intersection are parallel to the ND (normal direction), as shown in Fig. 7(c). Moreover, the grains near the fusion line grow in a specific direction (perpendicular to the fusion line) on both the 304 side and the Q235B side. Compared with the fusion zone of 304

stainless steel, the grain sizes in the Q235B fusion zone are highly uneven and relatively large.

Information on the four elements (Cr, Fe, C, and Ni) at the location of the fusion zones was acquired by using SEM and energy-dispersive spectroscopy (EDS), as shown in Fig. 8. Figure 8(a) shows that the proportions of the four elements on the Q235B side vary greatly, i.e., Fe decreases considerably and Cr clearly increases, while C and Ni slightly decrease and increase, respectively. Furthermore, a transition zone of approximately 25 μm is defined according to the enhancement

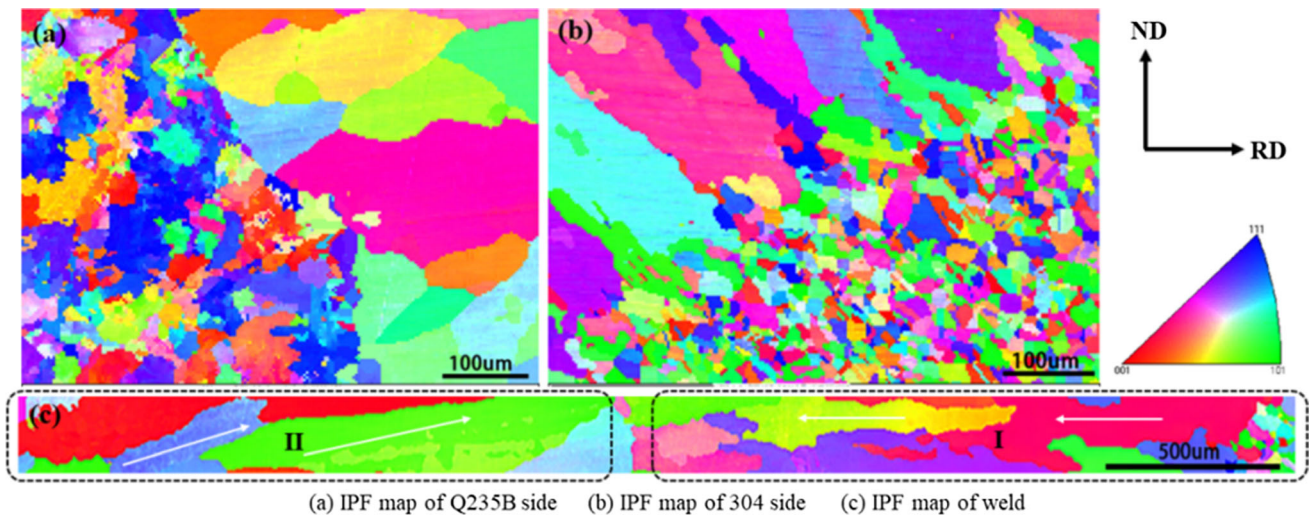


Fig. 7 Microstructure of welded joint

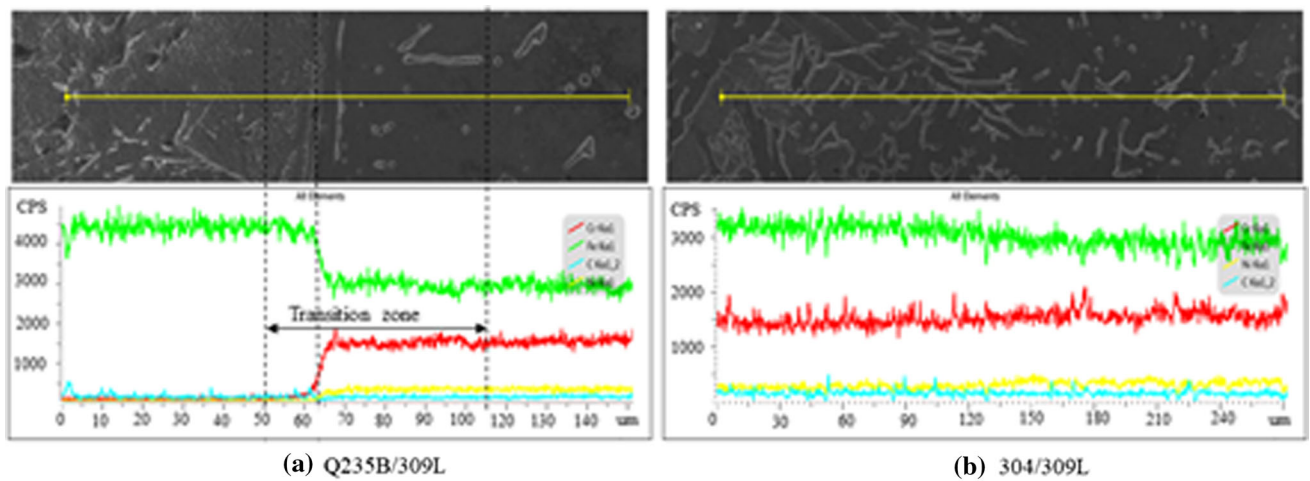


Fig. 8 EDS results of a welded joint

of elemental Fe. Compared with Fig. 6(b), part of the transition region is observed in the martensite layer. At the 309L/304 interface, because the difference in the composition of the filler metal 309L and the base metal 304 stainless steel is not obvious, the elemental transition is not obvious. Elemental Fe decreases slightly during the transition from the base metal to the filler metal, while the contents of Cr and Ni increase slightly, as shown in Fig. 8(b).

In Fig. 9, it can be observed that the microstructure of the weld is worm-like domains with skeletal distribution of ferrite in austenite. According to the WRC-1992 constitution diagram (Ref 19), the ferrite formation is FA mode. The transformation from δ ferrite to γ austenite consumes many austenite elements, such as Ni and Mn, and ferritic elements, such as Cr and Mo, remain in base δ ferrite. Therefore, ferrite nuclei are retained, and the growth of austenite limits its diffusivity. With decreasing temperature, worm-like domains and/or stable skeletal ferrite structures form (Ref 1, 19). The EDS results in Fig. 9 clearly show Cr-rich and Ni-poor composition in the ferritic area compared with austenite in the weld.

3.3 Mechanical Properties

3.3.1 Tensile Properties and Fracture Morphologies. The results of axial tensile tests at room temperature are illustrated in Fig. 10. The average tensile strength of the welded joint is 534 MPa, which is almost the same as that of the Q235B base metal but much smaller than that of the 304 base metal. Notably, the average elongation of the welded joints is much less than that of Q235B and 304.

After the tensile tests, the fracture surfaces were preserved with plastic film and observed by SEM. The macroscopic morphology of the tensile specimens after fracture is shown in Fig. 11(a). All the fractures take place in the weld zone, and obvious examples of necking are present at the fractures. The SEM image (Fig. 11(b)) of the fracture surface of a welded joint show dimples with uniform equiaxial size and tiny secondary particles, which indicates ductile fracture and consistent grain distribution at the fractured weld. Moreover, dimples of varied sizes and depths are observed at the fracture surface of 304 base metal (Fig. 11(c)), whereas the fracture surface of Q235B base metal manifests few dimples and cleavage steps formed by

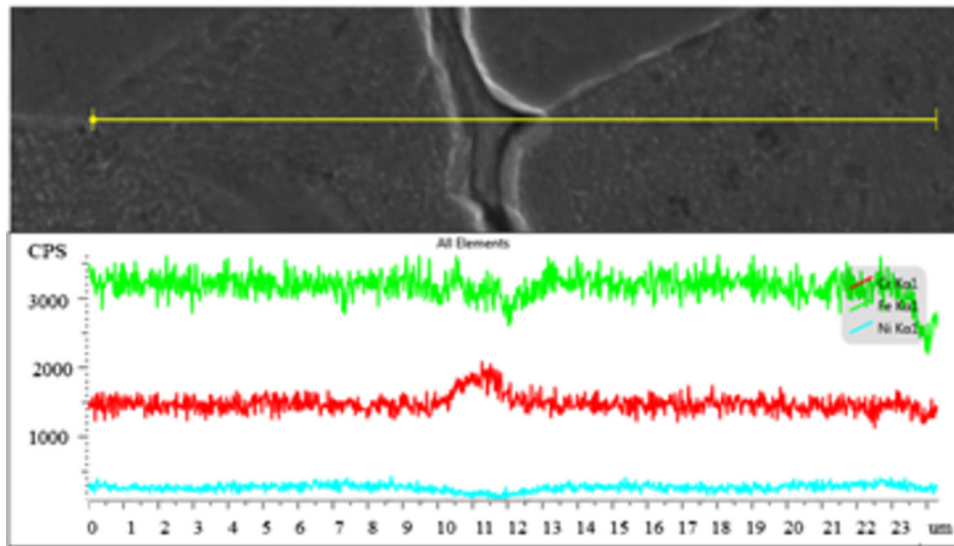


Fig. 9 EDS scan of ferrite at the weld seam

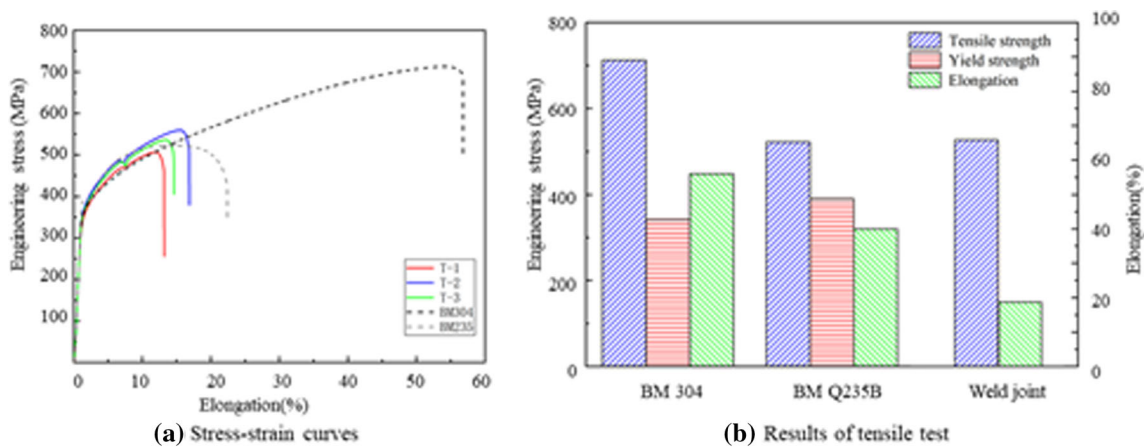


Fig. 10 Results of tensile tests

crystal faces at different heights (Fig. 11(d)), which are evidence of brittle fracture.

3.3.2 Microhardness Distribution. The microhardness distribution of the transverse section of the welded joint is depicted in Fig. 12. The three variation curves in Fig. 12(a) correspond to the microhardness distributions of the top, middle, and bottom of the weld. Moreover, a matrix algorithm was utilized to analyze the data, and a microhardness distribution map was obtained. Compared with the microhardness distributions of the top, middle, and bottom of the weld, the microhardness of the middle region corresponds to the greatest change and the widest region of low hardness. The microhardness distribution maps of the welded joint in Fig. 12 (b) share the same shape as that of the molten pool, as shown in Fig. 3(a). The average microhardness of BM304 and BMQ235B is approximately 200 and 170 $HV_{0.5}$, respectively. The microhardness at the weld is quite low, with an average value of approximately 160 $HV_{0.5}$. In the HAZ304 area, the microhardness is much lower than that of the 304 base metal due to the coarse grain size. However, the microhardness at the Q235B fusion line is relatively high, up to 304 $HV_{0.5}$, resulting from

the hard martensite structure, as illustrated in Fig. 6(c). Furthermore, the microhardness values of CGHAZQ235B and FGHAZQ235B are much higher than that of BMQ235B. There are several reasons for this result. First, the presence of a Widmanstatten structure dominates in CGHAZQ235B, as shown in Fig. 3(b) and (c). Second, grain refinement in FGHAZQ235B determines the high value of the microhardness, as shown in Fig. 3(d). Third, the microhardness of IGHZAQ235B is much lower because of its uneven structure and coarse ferritic grain structure.

Notably, the microhardness is lowest at the centerline of IGHZAQ235B (approximately 150 $HV_{0.5}$), the upper and bottom lines in IGHZAQ235B (approximately 160 $HV_{0.5}$), and the welded center (also approximately 160 $HV_{0.5}$). Moreover, the microhardness distribution maps (Fig. 12(b)) show that the microhardnesses of the welded center and IGHZAQ235B are almost the same throughout the vertical direction, thus indicating that the tensile specimens were prone to fracture at these two positions in axial tensile tests. However, Fig. 11(a) shows that all the fractures take place in the weld zone; the fracture mechanisms are discussed in detail in the Discussion section.

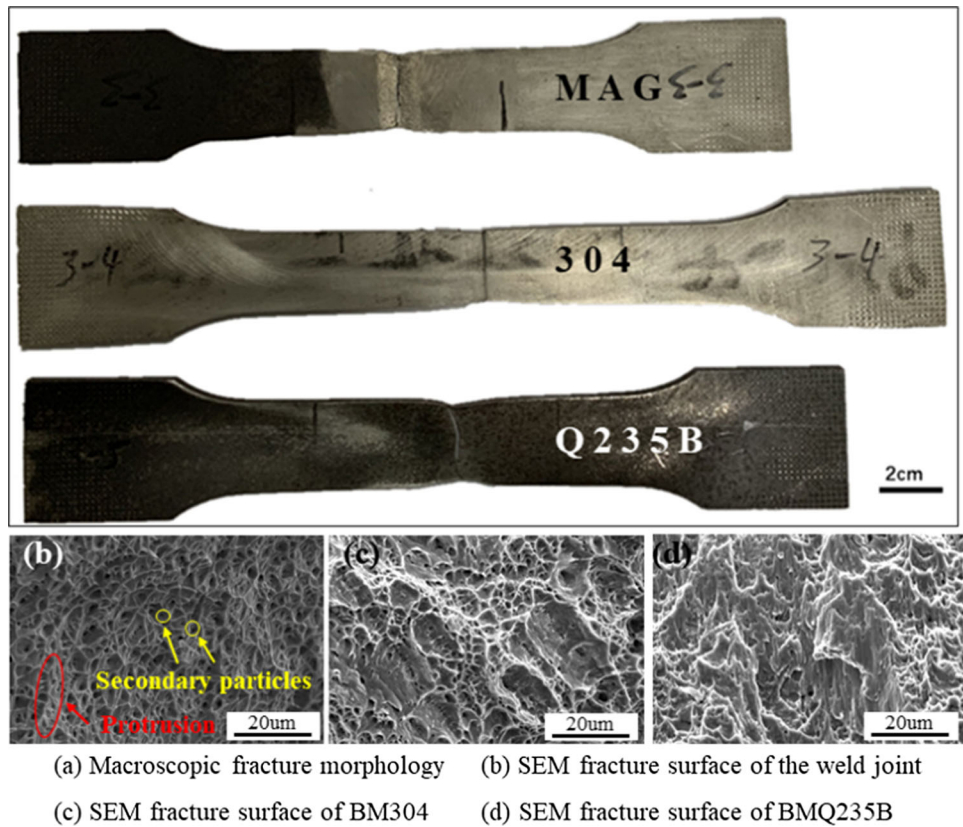


Fig. 11 Location of fracture in a tensile specimen and SEM image of the fracture surface

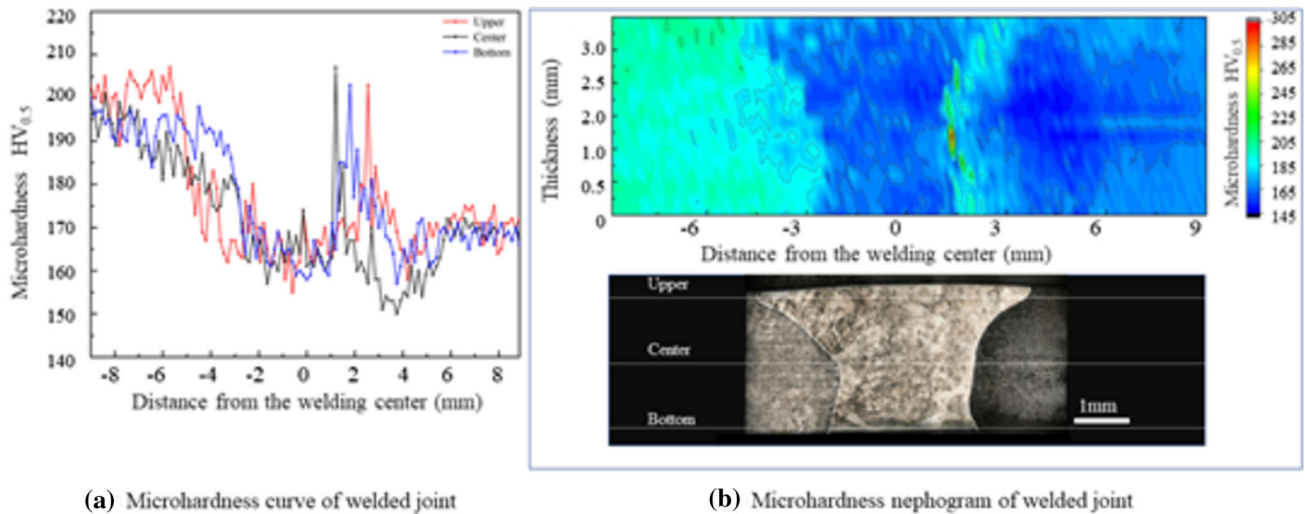


Fig. 12 Microhardness distribution of the welded joint

4. Discussion

Generally, the mechanical properties of a welded joint are always determined by its microstructure and chemical composition, and the microstructure and elemental segregation of a welded joint are affected by the thermal gradient and cooling rate (Ref 20, 21). Moreover, the thermal gradient and cooling rate dominate the melting and solidification behaviors of the welded joint. Thus, it is essential to understand the melting and solidification of welded joints to judge the mechanical prop-

erties of welded joints. According to published research on dissimilar steel welding, tensile fracture is mainly concentrated in the heat-affected zone of carbon steel (Ref 22–25). Some scholars believe that the asymmetric deformation of welded joints is caused by nonuniform microstructures in the heat-affected zone that eventually lead to tensile fracture of the weld joint (Ref 22, 26, 27). However, in the present work, the fracture locations in the welded joints are at the welds in the tensile tests, as shown in Fig. 11(a). To reveal the failure mechanism, the solidification and crystallization behaviors of

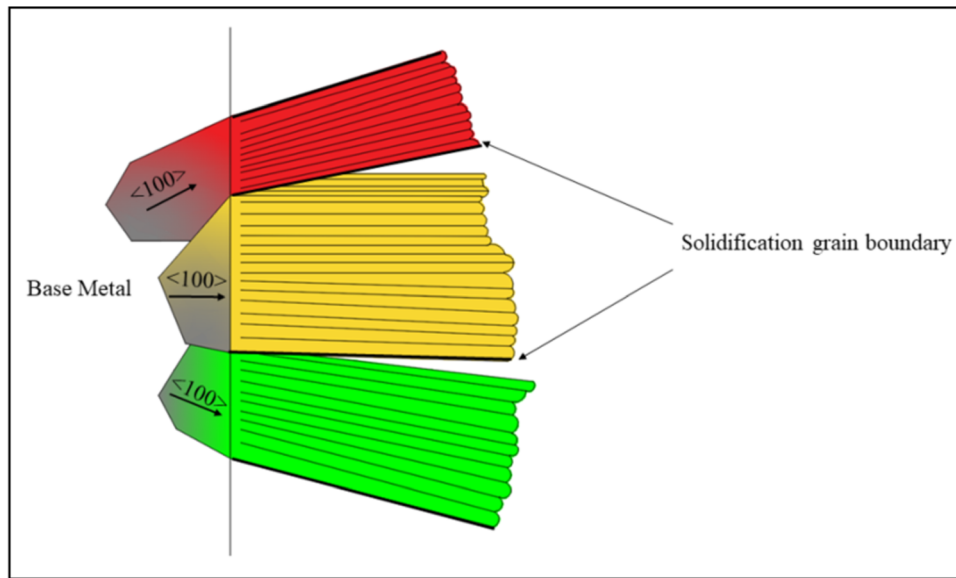


Fig. 13 Schematic diagram of grain growth

the welded joints were analyzed in detail, and the coherent relationships between the microstructure, mechanical properties and solidification and crystallization behaviors were clarified.

As the thermal conductivity of 304 austenitic stainless steel is much lower than that of Q235B low carbon steel, the heat conduction of the 304 stainless steel side is slower during the welding process, and more molten metal is produced at the 304 stainless steel side in the molten pool. Under the influence of gravity, the liquid metal in the molten pool flows downward, and the metal at the bottom of the molten pool gradually melts as it is exposed to heat. As a result, the shape of the molten pool gradually elongates, and the molten pool changes from an ellipse to water droplets. As shown in Fig. 4(a) and 5(a), the shape of the fusion line differs on both sides of the weld in the two base metals. The shape of the weld pool (the shape of the fusion line) has a great influence on the process of grain growth from the base metal to the weld center, which ultimately affects the mechanical properties of the weld joint (Ref 28, 29).

Once the temperature becomes lower than the melting point, the base metal at the edge of the molten pool (fusion line) begins to solidify into a dendrite. The structure of the filler metal of GMS-309L is fcc (face-centered cubic), and solidification preferentially proceeds along the cube edge or in the $\langle 100 \rangle$ crystallization (Ref 30) direction, the direction of easy growth, as shown in Fig. 13. When the easy growth direction is parallel to the heat flow vector and perpendicular to the isotherm of the solid-liquid interface, solidification growth is the easiest. Therefore, the grain direction at the weld differs, and all grain growth is perpendicular to the solid-liquid interface (Fig. 7), which is consistent with the grain solidification direction, until a grain contacts the solid-liquid interface or a preferential grain position in the metal adjacent to the weld. The grain growth diagram for dissimilar metal welding (carbon steel and stainless steel) is depicted in Fig. 14. As shown in Fig. 14(a), for the columnar grains in the Q235B low carbon steel side of the weld, with grain growth extending from the side of the Q235B to the inside of the weld, the angle between

the velocity vector of grain solidification and the central heat flow direction gradually changes from vertical at the melting boundary to parallel near the weld center (Ref 31); this behavior can also be observed in region I in Fig. 7(c). However, as shown in Fig. 14(b), the columnar grains on the side of 304 stainless steel grow perpendicular to the boundary of the pool (the fusion line) due to the linear boundary of the droplet pool, which can also be observed in region II in Fig. 7(c).

As shown in Fig. 14, different grain growth behaviors on both sides of the weld are conducive to the head-on collision of columnar grains growing from both sides of the molten pool (Ref 32), and a continuous grain boundary parallel to the ND forms at the weld centerline, as shown in Fig. 14(c). Continuous grain boundaries parallel to the ND can be observed at different positions of the weld center from the EBSD images, as shown in Fig. 15.

Notably, the strain in fcc materials (filler metal: GMS-309L) tends to be concentrated at the grain boundaries rather than uniformly distributed throughout the microstructure (Ref 30). Thus, cracks easily initiate at the nearly linear grain boundaries displayed in Fig. 15 in the axial tensile tests. Moreover, the fracture resistance of the steels is always determined by their plastic deformation capacity, which is related to movement of the crystal and formation of slip bands. The nearly linear grain boundaries do not easily move and rotate during the slip process, thus resulting in a low plastic deformation capacity. When the welded joint is subjected to the transverse (RD) force in the axial tensile test, slip processes take place at the grain boundaries, and some small holes emerge between the grain boundaries. The aggregated and vertical grain boundaries lack binding, and cracks form here, finally resulting in fracture at the weld center. The fracture morphology of the welded joint displayed in Fig. 11(b) indicates that there are no obvious large depressions and voids in the equiaxed dimple, and there are protrusions that appear to be pulled out, which is due to the low plastic deformation ability of the material along the axial direction.

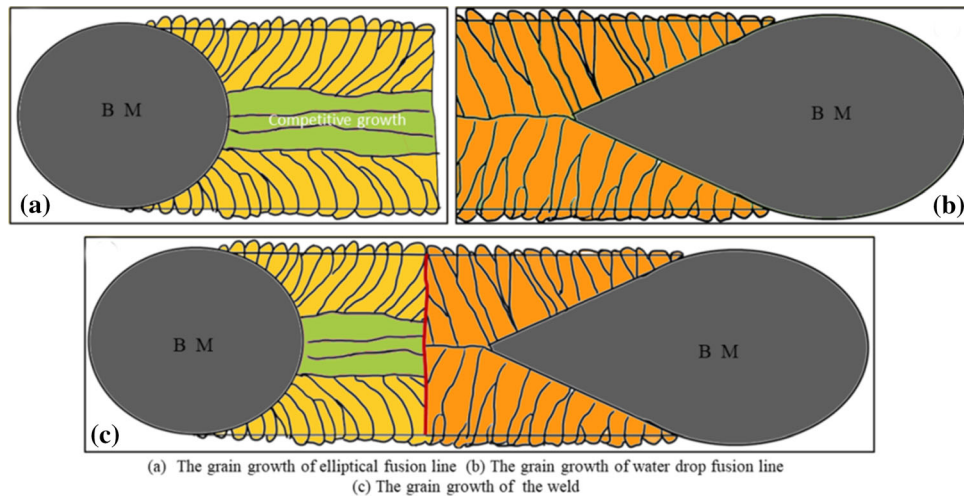


Fig. 14 Diagram of weld grain growth [26]

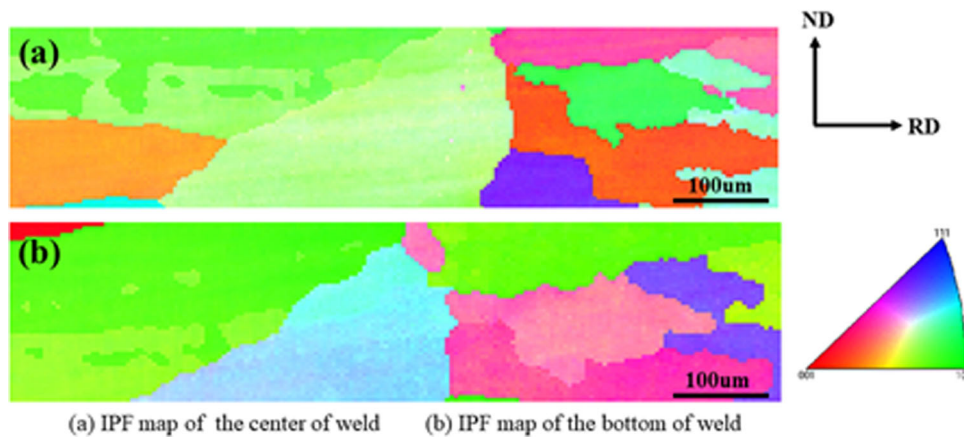


Fig. 15 Microstructure of center of a welded joint

5. Conclusions

The dissimilar welding of 304 stainless steel and Q235B low carbon steel was conducted by using MAG, and the microstructure and mechanical properties of the welded joints were studied. The relationships among the mechanical properties, microstructure, and condensation mode were explored based on the condensation mode of the welded joint. According to the obtained results, the following conclusions were drawn:

- (1) The welding joints were complete with no defects, such as slag inclusions, cracks, porosity, nonpenetration, and nonfusion. The weld microstructure was organized with worm-like domains and skeletal ferrite distributed in the austenite grains. Due to the influence of heat conduction and the heat cycle, grain coarseness occurred in the heat-affected zone of the Q235B carbon steel and 304 stainless base metals. The structure of the heat-affected zone on the carbon steel side was complicated, including Wissler structure, pearlite and ferrite.
- (2) The grain size at the weld seam was relatively large, and the grain boundaries at the intersection were parallel to the ND. Moreover, the grains near the fusion line grew in a specific direction (perpendicular to the fusion

line) on both the 304 side and the Q235B side. EDS results indicated that the proportions of the four main elements varied greatly in the Q235B side of the weld; however, the elemental transition was not obvious in the 304 side. In addition, Cr-rich and Ni-poor behaviors were clear in the ferritic areas.

- (3) The tensile strength of the welded joint was slightly larger than those of Q235B carbon steel, and the form of the welded joint was equal strength matching. All the fractures of the welded joints take place in the weld zone, and obvious examples of necking are present at the fractures.
- (4) The microhardness in the middle region of the weld showed the greatest change with the widest region of low hardness. The microhardness was much less in the HAZ304 area than in the 304 base metal due to the coarse grain size. However, the microhardness values of CGHAZQ235B and FGHAZQ235B were much greater than that of BMQ235B due to Widmanstatten structure and grain refinement, respectively. Martensite in the transition area resulted in the greatest hardness near the fusion line on the carbon steel side in the welded joint.
- (5) Because of the different thermal conductivities of the base metals, the different shapes of the molten pool on both sides of the weld resulted in the formation of solid-

ification grain boundaries in the center of the weld during welding. This area was vulnerable to the formation of solidification cracks in welds and resulted in weld fracture in tensile tests.

According to this study, the ultimate cause of welding failure was the difference in the thermal conductivities of the hot base metals and excessive heat input. Further work will be needed to obtain better performance of welded structures by improving welded joints of dissimilar steels through changes in the process (current, welding speed, shielding gas) as well as the welding position.

Funding

The work was supported by the Guangdong Basic and Applied Basic Research Foundation (No. 2019A1515110807) and the Youth Innovation Talents Project of Guangdong Provincial Department of Education (No. 2018KQNCX271).

Conflict of interest

The authors declare that they have no conflict of interest. If accepted, the article will not be published elsewhere in the same form, in any language, without the written consent of the publisher. All authors have participated sufficiently in this work to take public responsibility for it, and all authors have reviewed the final version of the manuscript and approved it for publication.

References

1. J. Zhang, Y. Huang, D. Fan et al., Microstructure and Performances of Dissimilar Joints between 12Cr2Mo1R Steel and 06Cr18Ni11Ti Austenitic Stainless Steel Joined by AA-TIG Welding, *J. Manuf. Process.*, 2020, **60C**, p 96–106.
2. A.R. Khalifeh, A. Dehghan and E. Hajjari, Dissimilar Joining of AISI 304L/St37 Steels by TIG Welding Process, *Acta Metall. Sin.*, 2013, **26(6)**, p 721–727.
3. H. Wang, K. Wang, W. Wang et al., Microstructure and Mechanical Properties of Dissimilar Friction Stir Welded Type 304 Austenitic Stainless Steel to Q235 Low Carbon Steel, *Mater. Charact.*, 2019, **155**, p 109803.
4. A. Khodadadi, M. Shamanian and F. Karimzadeh, Microstructure and Mechanical Properties of Dissimilar Friction Stir Spot Welding between St37 Steel and 304 Stainless Steel, *J. Mater. Eng. Perform.*, 2017, **26(6)**, p 2847–2858.
5. W.W. Zhang and S. Cong, Process Optimization and Performance Evaluation on Laser Beam Welding of Austenitic/Martensitic Dissimilar Materials, *Int. J. Adv. Manuf. Technol.*, 2017, **92(9)**, p 4161–4168.
6. C. Köse, Dissimilar Laser Beam Welding of AISI 420 Martensitic Stainless Steel to AISI 2205 Duplex Stainless Steel: Effect of Post-Weld Heat Treatment on Microstructure and Mechanical Properties[J], *J. Mater. Eng. Perform.*, 2021, **30**, p 1–32.
7. H.Y. Huang, Effects of Activating Flux on the Welded Joint Characteristics in Gas Metal Arc Welding, *Mater. Des. (1980-2015)*, 2010, **31(5)**, p 2488–2495.
8. L. Liang, X. Wenkai, Z. Jiaqi et al., Microstructure and Cryogenic Toughness of 316LN Austenite Stainless Steel Weld Metal Welded by NG-MAG Arc Welding[C], *J. Phys.: Conf. Ser.*, 2020, **1699(1)**, p 012027.
9. Z.M. Cao, G.F. Zhang, J.M. Zhang et al., Evolution of MA Constituents in HAZ and its Effect on Toughness of MAG Joint of Granular Bainitic Steel Q690C, *J. Mech. Eng.*, 2014, **50(20)**, p 84.
10. P.R. Spena, F. D'Aiuto, P. Matteis et al., Dissimilar Arc Welding of Advanced High-Strength Car-Body Steel Sheets [J], *J. Mater. Eng. Perform.*, 2014, **23(11)**, p 3949–3956.
11. K. Kimapong and S. Triwanapong, Effect of GMAW Shielding Gas on Tensile Strength of Dissimilar SS400 Carbon Steel and SUS304 Stainless Steel Butt Joint[C] Materials Science Forum, *Trans. Tech. Publ. Ltd*, 2019, **950**, p 70–74.
12. D.K. Singh, G. Sahoo, R. Basu, V. Sharma and M.A. Mohtadi-Bonab, Investigation on the Microstructure—Mechanical Property Correlation in Dissimilar Steel Welds of Stainless Steel SS 304 and Medium Carbon Steel EN 8, *J. Manuf. Process.*, 2018, **36**, p 281–292.
13. Y.U. Fengyi, W.E.I. Yanhong and L.I.U. Xiangbo, The Evolution of Polycrystalline Solidification in the Entire Weld: A Phase-Field Investigation, *Int. J. Heat Mass Transf.*, 2019, **142**, p 118450.
14. D.W. Rathod, S.K. Sharma, S. Pandey, Hot Cracking Susceptibility: An Effect of Solidification Modes of SS Consumables During Bimetallic Welds. In: *Optimization Methods in Engineering*. Springer, Singapore, 2021. p 537–547
15. Z.R. Chen, Y.H. Lu, X.F. Ding et al., Microstructural and Hardness Investigations on a Dissimilar Metal Weld Between Low Alloy Steel and Alloy 82 Weld Metal, *Mater. Charact.*, 2016, **121**, p 166–174.
16. Q. Wang, M. Zhang, W. Liu et al., Cr or C Controlled Formation of Transition Martensite in Dissimilar Metal Weld, *Mater. Charact.*, 2019, **147**, p 434–442.
17. T.W. Nelson, J.C. Lippold and M.J. Mills, Nature and Evolution of the Fusion Boundary in Ferritic-Austenitic Dissimilar Weld Metals, Part 1—Nucleation and Growth, *Weld. J.-New York*, 1999, **78**, p 329–s.
18. T.W. Nelson, J.C. Lippold and M.J. Mills, Nature and Evolution of the Fusion Boundary in Ferritic-Austenitic Dissimilar Metal Welds—part 2: On-Cooling Transformations, *Weld. Res.*, 2000, **10**, p 267–277.
19. A. Moteshakker and I. Danaee, Microstructure and Corrosion Resistance of Dissimilar Weld-Joints between Duplex Stainless Steel 2205 and Austenitic Stainless Steel 316L, *J. Mater. Sci. Technol.*, 2016, **32(003)**, p 282–290.
20. H. Xu, M.J. Xu, C. Yu et al., Effect of the Microstructure in Unmixed Zone on Corrosion Behavior of 439 Tube/308L Tube-Sheet Welding Joint, *J. Mater. Process. Technol.*, 2017, **240**, p 162–167.
21. L. Mujica, S. Weber, H. Pinto et al., Microstructure and Mechanical Properties of Laser-Welded Joints of TWIP and TRIP Steels, *Mater. Sci. Eng.*, 2010, **527(7–8)**, p 2071–2078.
22. Y. Huang, L. Zhen, L. Yuchen et al., Dissimilar Joining of AISI 304/Q345 Steels In Keyhole Tungsten Inert Gas Welding Process, *Int. J. Adv. Manuf. Technol.*, 2018, **96(9–12)**, p 4041–4049.
23. X. Liu, F. Lu, R. Yang et al., Investigation on Mechanical Properties of 9%Cr/CrMoV Dissimilar Steels Welded Joint[J], *J. Mater. Eng. Perform.*, 2015, **24(4)**, p 1434–1440.
24. N. Arivazhagan, S. Singh, S. Prakash et al., Investigation on AISI 304 Austenitic Stainless Steel to AISI 4140 low Alloy Steel Dissimilar Joints by Gas Tungsten Arc, Electron Beam and Friction Welding, *Mater. Des.*, 2011, **32(5)**, p 3036–3050.
25. X. Zhang, Y. Zhang et al., Effects of Melting-Mixing Ratio on the Interfacial Microstructure and Tensile Properties of Austenitic-Ferritic Stainless Steel Joints-ScienceDirect, *J. Mater. Res. Technol.*, 2019, **8(3)**, p 2649–2661.
26. N. Farabi, D.L. Chen and Y. Zhou, Microstructure and Mechanical Properties of Laser-Welded Dissimilar DP600/DP980 Dual-Phase Steel Joints, *J. Alloy. Compd.*, 2011, **509(3)**, p 982–989.
27. A. Ozlati, M. Movahedi and H. Mohammadkamal, Upset Resistance Welding of Carbon Steel to Austenitic Stainless Steel Narrow Rods, *J. Mater. Eng. Perform.*, 2016, **25(11)**, p 1–9.
28. J.C. Lippold, *Welding Metallurgy and Weldability*, Wiley, Hoboken, 2014, p 13–57
29. B.T. Alexandrov, J.C. Lippold, J.W. Sowards et al., Fusion Boundary Microstructure Evolution Associated with Embrittlement of Ni-base Alloy Overlays Applied to Carbon Steel, *Weld. World*, 2013, **57(1)**, p 39–53.
30. W.D. Callister, D.G. Rethwisch, A. Blicblau et al., *Materials science and engineering: an introduction[M]*, Wiley, 2021, p 314–325
31. D.J. Kotecki and T.A. Siewert, WRC-1992 Constitution Diagram for Stainless Steel Weld Metals: A Modification of the WRC-1988 Diagram, *Weld. J.*, 1992, **71(5)**, p 171–178.
32. S. Kou, *Welding metallurgy[M]*, Wiley, 2003, p 145–212

Publisher's Note Springer Nature remains neutral with regard to jurisdictional claims in published maps and institutional affiliations.